RESEARCH ARTICLE
SOLID EARTH: EXPLORATION GEOPHYSICS

Earth and Planetary Physics
10: 57–74, 2026
doi: 10.26464/epp2026001

Geothermal prospecting through integrated CSAMT and soil radon methods in Baozigou village, Yuncheng Basin, Fenwei Rift, China

GuoPeng Wu[1], HuiYou He[2,3,4,5*], GuoXiong Chen[6], XiaoRong Ren[7], JiFeng Zhang[8], and Yang Gao[9]

[1]Shanxi Province Intelligent Optoelectronic Sensing Application Technology Innovation Center, Yuncheng University, Yuncheng Shanxi 044000, China;
[2]School of Mathematics and Statistics, Huanggang Normal University, Huanggang Hubei 438000, China;
[3]State Key Laboratory of Precision Geodesy, Innovation Academy for Precision Measurement Science and Technology, CAS, Wuhan 430071, China;
[4]Engineering Research Center of Natural Resource Information Management and Digital Twin Engineering Software, Ministry of Education, Wuhan 430074, China;
[5]Hubei Key Laboratory of Intelligent GeoInformation Processing, China University of Geosciences, Wuhan 430074, China;
[6]State Key Laboratory of Geological Processes and Mineral Resources, China University of Geosciences, Wuhan 430074, China;
[7]Renxing New Energy Technology Limited Corporation, Hejin Shanxi 043300, China;
[8]School of Geology Engineering and Geomatics, Chang'an University, Xi'an 710054, China;
[9]China Nonferrous Metal Mining (Group) Corporation Limited, Beijing 100029, China

Key Points:

- A combination of CSAMT and radon methods was utilized to delineate the subsurface geothermal structure and possible thermal-controlling faults in Baozigou village, Yuncheng Basin, Shanxi Rift.
- Our results suggest that the Quaternary and Neogene clastics function as the geothermal cap, whereas the Paleogene sandstones and the Lower Ordovician and Cambrian limestones constitute the deep reservoirs in Baozigou village, with two newly identified normal faults as potential conduits of geothermal fluids.
- A preliminary geothermal conceptual model of the Fen River Depression was further developed, which supports the process of locating a new deep geothermal drilling site in the northwest of the Baozigou village.

Citation: Wu, G. P., He, H. Y., Chen, G. X., Ren, X. R., Zhang, J. F., and Gao, Y. (2026). Geothermal prospecting through integrated CSAMT and soil radon methods in Baozigou village, Yuncheng Basin, Fenwei Rift, China. *Earth Planet. Phys.*, *10*(1), 57–74. http://doi.org/10.26464/epp2026001

Abstract: The Yuncheng Basin, located in the southern part of the Fenwei Rift, North China, exhibits obvious crust thinning (Moho uplift of 6–8 km) and shallow Curie point depth (less than 18 km) and hence holds great potential for geothermal resources. However, geothermal exploration within the Yuncheng Basin typically faces significant challenges due to civil and industrial noise from dense populations and industrial activities. To address these challenges, both Controlled-Source Audio-frequency Magnetotellurics (CSAMT) and radon measurements were employed in Baozigou village to investigate the geothermal structures and identify potential geothermal targets. The CSAMT method effectively delineated the structure of the subsurface hydrothermal system, identifying the reservoir as Paleogene sandstones and Ordovician and Cambrian limestones at elevations ranging from −800 m to −2500 m. In particular, two concealed normal faults (F_a and F_b) were newly revealed by the combination of CSAMT and radon profiling; these previously undetected faults, which exhibit different scales and opposing dips, are likely to be responsible for controlling the convection of thermal water within the Basin's subsurface hydrothermal system. Moreover, this study developed a preliminary conceptual geothermal model for the Fen River Depression within the Yuncheng Basin, which encompasses geothermal heat sources, cap rocks, reservoirs, and fluid pathways, providing valuable insights for future geothermal exploration. In conjunction with the 3D geological model constructed from CSAMT resistivity structures beneath Baozigou village, test drilling is recommended in the northwestern region of the Baozigou area to intersect the potentially deep fractured carbonates that may contain temperature-elevated geothermal water. This study establishes a good set of guidelines for future geothermal exploration in this region, indicating that high-permeability faults in the central segments of the Fen River Depression are promising targets.

Keywords: controlled source audio-frequency magnetotellurics; soil radon; geothermal exploration; Fenwei Rift; conceptual model

First author: G. P. Wu, guopeng_wu@126.com
Correspondence to: H. Y. He, huiyouhe@163.com
Received 26 APR 2025; Accepted 20 JUL 2025.
First Published online 22 AUG 2025.

1. Introduction

The heat or thermal energy of the Earth exceeds the energy of all known traditional resources of coal, oil, and natural gas, and could contribute a lot by modifying the carbon cycle and reducing greenhouse gas emissions (Boden, 2016). Despite its potential, geothermal energy has been overshadowed by solar and wind in recent years (Li KW et al., 2015; Bolinger et al., 2023). The primary obstacle to widespread adoption of geothermal energy is its non-uniform distribution; specific geologic conditions and processes allow its exploitation. As several studies indicate, potential geothermal resources typically develop in regions of active magmatism and/or crustal thinning (e.g., Moeck, 2014; Wang GL and Lin WJ, 2020; Jolie et al., 2021). The investigation and exploitation of untapped geothermal reservoirs hold significant potential for augmenting electricity and thermal energy provisions.

In China, high-temperature geothermal fields are found mostly within the Himalayan and Circum-Pacific tectonic belts; moderate- and low-temperature resources are situated predominantly in Eastern China (Zhu JL et al., 2015; Wang GL et al., 2017). The Cenozoic Fenwei Rift in Eastern China, just like the East African Rift, induced a large increase of mantle heat flow beneath continents, yielding several famous and promising geothermal reservoirs, such as the northern Yanggao–Tianzhen and the southwestern Xianyang–Xi'an geothermal fields (He LP et al., 2021). In the Yanggao–Tianzhen geothermal field, geothermal fluids with a measured bottomhole temperature (BHT) of 160.2 °C at a depth of 1624.01 m have been explored and utilized to generate electricity with a small installed capacity of about 600 kW (Zhou WL, 2021). The Xianyang–Xi'an geothermal fields, characterized by porous sandstone reservoirs, have been exploited for urban space heating over the past years (Erlingsson et al., 2010; Kong YL et al., 2014; Ke TT et al., 2021). Studies indicate that the dominant mechanism of heat transfer in the Fenwei Rift geothermal systems consists of both heat conduction through the thinned crust and heat advection along deep fault boundaries (Wang GL and Lin WJ, 2020; Ren ZL et al., 2020; Zhou WL et al., 2020). This mechanism may be further augmented by the presence of an uncooled magma chamber in the shallow upper crust, which makes the Yanggao–Tianzhen area the only high-temperature geothermal field identified in the Fenwei Rift to date (Rao et al., 2016; Zhou WL et al., 2022). The Yuncheng Basin in the southern part of the Fenwei Rift has the most obvious crust thinning (Moho uplift of 6–8 km) and shallowest values of Curie point depths (less than 18 km) among that region's sub-grabens (such as Taiyuan, Datong), thereby holding greatest geothermal potential (Chen YF et al., 2021; Li Z et al., 2023). Since 2008, Yuncheng geothermal fields, which contain both carbonate and sandstone geothermal reservoirs, have been utilized for small-scale urban district heating. However, in 2017, most geothermal wells were shut down mainly due to large water head declines resulting from the absence of reinjection practices (Li Q, 2015; Qiao JW et al., 2018). With increasing emphasis on geothermal development and utilization both in China and globally, along with advancements in reinjection technology, geothermal development in Yuncheng Graben is poised for significant progress. We suggest that it is now imperative to establish a solid foundation for future geothermal development by employing appropriate geological and geophysical methods to identify potential geothermal reservoirs.

During the exploration of geothermal resources, thermal and electrical (resistivity) information, which are directly influenced by geothermal activity, are always the first target parameters (Georgsson, 2009). Especially, the electrical conductivity of the subsurface can effectively characterize the geothermal system, including hydraulic faults, heat sources, and geothermal reservoirs, which are ideal targets for electromagnetic (EM) or traditional direct current (DC) resistivity methods (Muñoz, 2014; He LF et al., 2016; Liu HY et al., 2022; Xie CL et al., 2024). Additionally, the subsurface resistivity structures in geothermal systems always reflect the characteristic hydrothermal alterations that allow for estimating temperatures (Ussher et al., 2000; Armadillo et al., 2020; Didas et al., 2024). Compared with DC resistivity methods, EM methods don't require physical intrusive contact with the ground, resulting in cost savings and increased efficiency. Based on the source of electromagnetic energy, EM methods can be classified either as passive, utilizing natural signals, or active, employing artificial transmitters.

Among these methods, Controlled-Source Audio-frequency Magnetotelluric (CSAMT) methods utilize artificial electromagnetic sources to actively investigate subsurface electrical structures with high anti-interference ability and good penetration depth (Hu XY et al., 2013). CSAMT has been applied widely and successfully in geothermal exploration all over the world, particularly in areas with significant cultural noise (e.g., Aykaç et al., 2015; Susilawati and Mustopa, 2019; Peng RH et al., 2023). However, CSAMT encounters the inherent ambiguity of any single survey method; it cannot fit all possible geological and environmental scenarios, which suggests the assistance of other complementary geophysical methods.

The radon soil gas survey method is innovative, rapid, and cost-effective; it can effectively identify high-permeability and fluid-conducting fault zones, which typically play a crucial role in hydrothermal geothermal fields (Baubron et al., 2002). This technique is based on the principle that high-permeability fault zones are commonly associated with anomalous fluxes of various gases, including CO_2, He, H_2, and radon (Davidson et al., 2016). In recent years, radon soil gas surveys have increasingly played a key role in mapping buried or blind faults, supporting other geophysical methods (Sun JL et al., 2022).

This study is focused on the Baozigou village in the Yuncheng Basin, where a geothermal borehole has revealed a deep carbonate reservoir at a depth of 2180 m with a temperature of 72 °C. To delineate the subsurface geothermal structures and possible tectonics, we employed both CSAMT and radon techniques. Based on the interpreted results and other previous work, including drilling, geochemistry, regional gravity, and magnetic data, we have developed a preliminary geothermal conceptual model that provides valuable novel insights into how effective geothermal exploration and utilization in the Yuncheng Basin can proceed.

2. Geological, Geophysical, and Geothermal Settings

2.1 Regional Settings

As shown in Figure 1a, Yuncheng basin is situated in southwestern part of S-shaped Fenwei continental Rift, the crystalline basement of which belong to the Trans-North China Orogen (TNCO) between the Western Blocks and Eastern Blocks within North China Craton (Zhao GC et al., 2005). Fenwei Rift mainly develops in conjunction with the collisional interaction of the Indian and Eurasian plates during Cenozoic and is tectonically still active nowadays (Yin YT et al., 2017). In contrast to the Eastern Block with significantly thinned lithosphere (60–100 km) and the western Ordos Block with stable thick lithosphere (>200 km), Fenwei Rift is a narrow transition zone with 80 km thick lithosphere characterized by strong earthquakes, local crustal thinning, low-magnitude volcanic activities, and the coexistence of compressional and extensional deformation (Chen L et al., 2009; Zhang YQ et al., 2007; Xu HR et al., 2020). Main basin-controlling extensional faults usually occurred along the Yanshannian fold and thrust belts (Xu XW et al., 1993). Minor amounts of rift related magmas have reached the surface within Fenwei Rift in exception of Datong basin in the north (Xu XW and Ma XY, 1992). Magnetotelluric sounding profiles show that there exist horizontal low velocity bodies at upper, middle and lower crustal levels beneath the

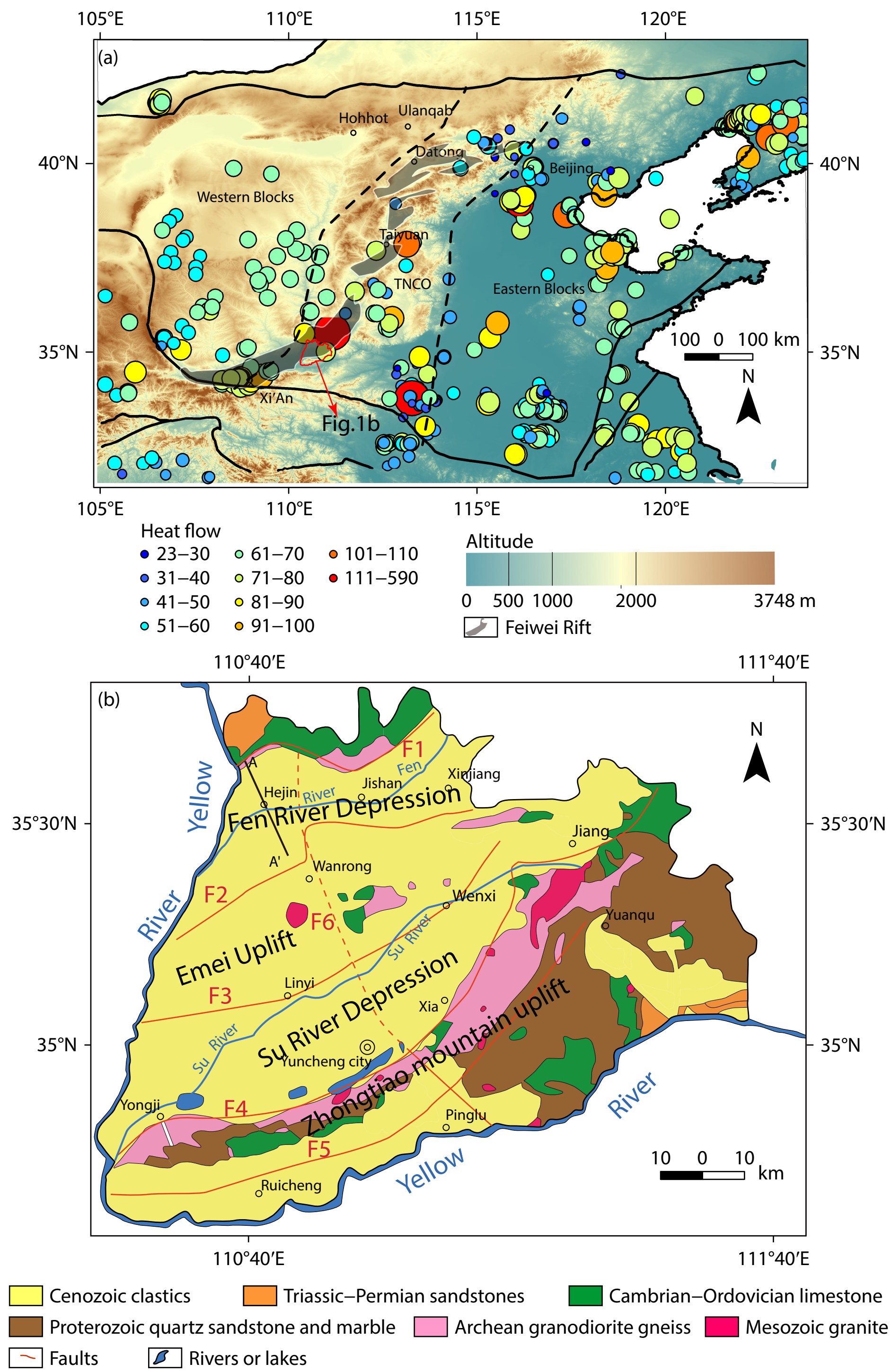

Figure 1. Tectonic subdivision and geological map, (a) Tectonic subdivision of the North China Craton (Zhao GC et al., 2005); (b) Simplified geological map of Yuncheng Basin.

Fenwei Rift, which were possibly caused by partial melting within the crust (Li ZH et al., 2014; Yin YT et al., 2017).

Geographically, Yuncheng Basin is bordered to the north by the Lüliang mountain, to the west by the Yellow River, and to the south and east by the Zhongtiao mountain (Figure 1b). Tectonically, Yuncheng Basin is composed of the Fen River Depression, Emei Uplift, and Su River Depression from north to south, which are mainly delineated and bounded by deep NE-trending faults. From north to south, these faults include the southern Lüliang mountain margin fault (F1), the northern Emei margin fault (F2), the southern Emei margin fault (F3), the northern Zhongtiao margin fault (F4), and the southern Zhongtiao margin fault (F5). Another significant normal fault, known as the Wanrong–Dongguo fault (F6), trends northwest and potentially intersects the major tectonic units and faults (Sun JY, 2016; Wang HY et al., 2025; Wu GP et al., 2025). However, F6 lacks clear surface expression and requires further investigation. The primary lithological units exposed within the Yuncheng Basin include Proterozoic metamorphic rocks, Lower Paleozoic carbonates, Cenozoic clastics, and minor Mesozoic granites, which are detailed in Table 1. The Cenozoic strata occupy 80% of the Yuncheng Basin and have a maximum thickness of up to 5 km in the south of the Su River Depression. A small number of Mesozoic granitic intrusions, primarily in the form of rock stocks, are located in Gu mountain and Canfang near Zhongtiao mountain (Qi Y et al., 2016).

The residual gravity and local magnetic fields in Figure 2 (obtained from regional-residual separation) depict the density and magnetic susceptibility distribution reflecting the associated geological information at shallow depths within the Yuncheng Basin. The densities and susceptibilities of the main rocks from the Yuncheng Basin can be referred to in Table 1. As shown in Figure 2a, the primary tectonic units of the Basin correspond to alternating low (the Fen River Depression), high (the Emei Uplift), and low (the Su River Depression) local gravity anomalies. Although both the Fen River Depression and the Su River Depression are NE-trending sedimentary subbasins, notable differences are evident in their local gravity (Figure 2a) and residual magnetic fields (Figure 2b). The Su River Depression features a single depression center, located in Yuncheng City, whereas the Fen River Depression contains two such centers, located in the Hejin and Jishan areas. Those two centers appear to be separated by an upcoming anomaly (M1) characterized by moderate gravity and high magnetic values (Figure 2b). M1 is interpreted to be a deep granitic intrusion, as Mesozoic granitoids are characterized by low density and high magnetic susceptibility in the Yuncheng Basin (see Table 1). Some drilling projects have uncovered the presence of intermediate-felsic granitic intrusive rocks beneath the Cambrian strata (Zhao B, 2013). Therefore, the basement rock in the Fen River Depression may be intruded by large-scale magnetic granites, which are not found in the Su River Depression. This M1 anomaly is situated in the northern part of the inferred F6. The NE-trending basin-controlling faults, including F1–F5, generally correspond to the gradients observed in local gravity and residual magnetic fields (Sun JY, 2016). In contrast, the NW-trending F6 fault crosscuts the main tectonic units and may be linked to deep granitoid intrusions within the Fen River Depression, as suggested by their spatial correlation.

In the Yuncheng Basin, only moderate- and low-temperature geothermal fields have been discovered to date. The Quaternary loose sediments are widely distributed and always act as an insulating cover layer, while the underlying Neogene–Paleogene sandstones and Cambrian–Ordovician limestones serve as geothermal reservoirs (Li Z et al., 2023). This geothermal pattern is prevalent across various geothermal fields in the Yuncheng Basin, including Hejin, Xinjiang, Jishan, Wanrong, and Linyi areas. However, in the center of the Su River Depression, where Cenozoic sediments reach depths of nearly 5 km, the reservoirs are composed primarily of Paleogene and/or Neogene sandstones. In the Fenwei Rift, the Yuncheng Basin exhibits the most significant crustal thinning, followed by the Linfen and Taiyuan Grabens (Chen YF et al., 2021). In addition, both the uplifted Moho and Curie isotherm surfaces beneath the Yuncheng Basin resulted in a thinned lithospheric thickness (Gao GM et al., 2015; Cai Y et al., 2021; Chen YF et al., 2021), suggesting promising geothermal potential for the Yuncheng Basin. Several studies have revealed that the NE-trending deep fault zones exert a controlling influence on the distribution of geothermal fields within the Yuncheng Basin (Li Z et al., 2023).

Table 1. Summary of primary geological strata and corresponding densities and susceptibilities in Yuncheng Basin (compiled using information from Zhao B, 2013; Sun JY, 2016 and Wang HY et al., 2025).

Geological strata	Density ($kg/m^3 \times 10^3$)		Susceptibility ($cgs \times 10^{-6}$)		Resistivity (Ωm)	
	Range	Average	Range	Average	Range	Average
Quaternary clays	1.50–1.91	1.67	0	0	20–100	30
Neogene siltstones	1.64–2.08	1.87	0	0	50–100	70
Paleogene mudstones and sandstones	1.88–-2.63	2.41	0	0	50–100	70
Triassic–Permian sandstones	2.35–2.70	2.55	0	0	50–250	150
Ordovician limestones	2.53–2.83	2.72	2–28	23	100–2000	600
Cambrian limestones	2.52–2.83	2.67	2–28	23	100–2000	600
Proterozoic quartz sandstone and marble	2.40–2.90	2.68	30–150	90	>1500	3000
Archean granodiorite gneiss	2.66–2.72	2.70	300–600	349	>1500	3000
Mesozoic granitoid	2.53–2.60	2.59	52–1200	647	200–4000	2000

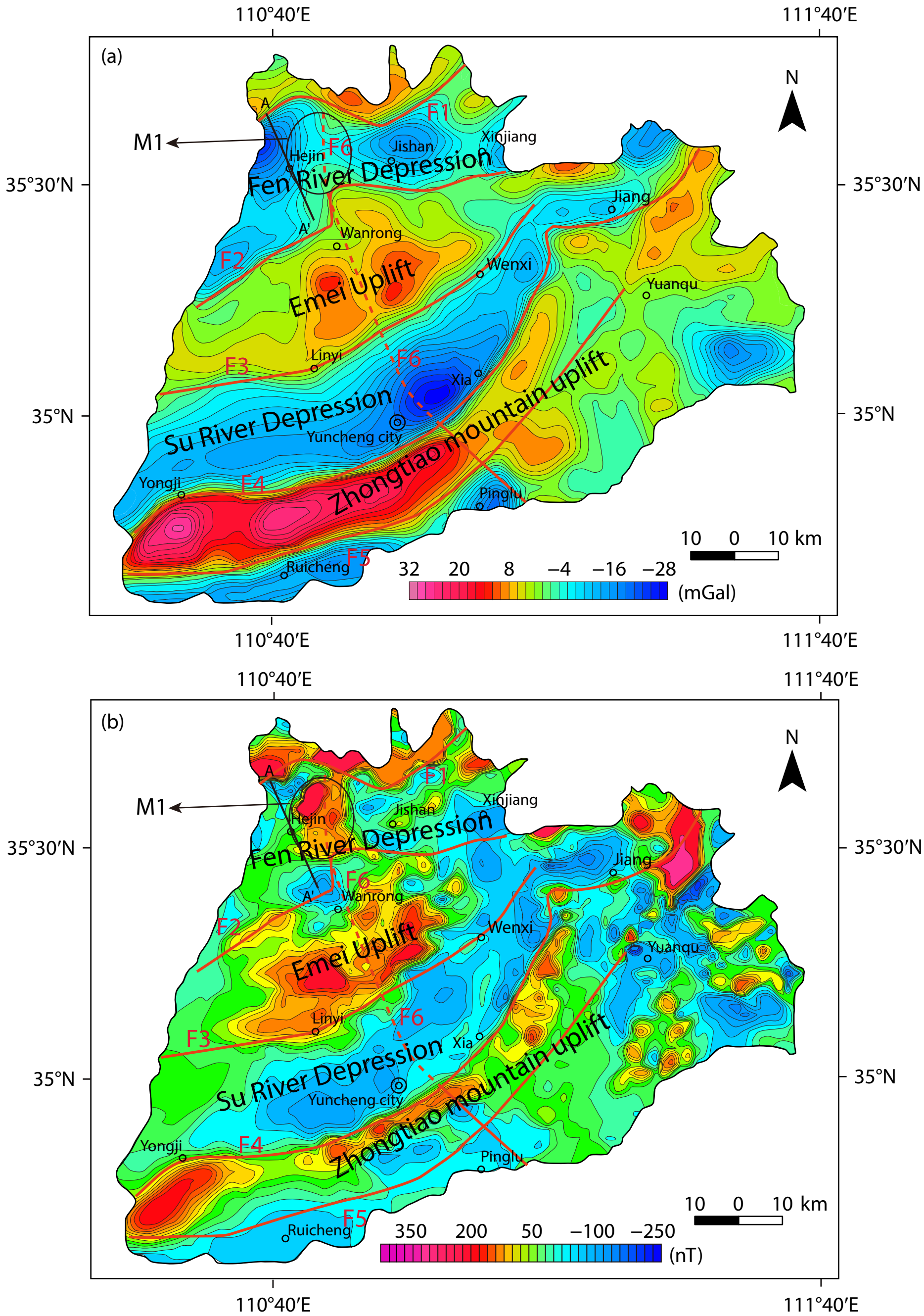

Figure 2. Anomaly maps of the study area. (a) The residual gravity anomaly; (b) the local magnetic anomaly (Sun JY, 2016), also showing the major interpreted faults.

2.2 Local Settings

The Hejin region is located in the western part of the Fen River Depression; both the Yellow River and the Fen River flow through this area. The F1 in the Hejin region is a curved boundary fault with a strike varying from NE to WNW as it extends from west to east. There are no obvious surface geothermal manifestations other than some cold springs near the foot of Lüliang mountain. The carbonate reservoirs in the Hejin region are characterized by an optimal depth (about 2 km), which facilitates a large water volume and ease of reinjection. Consequently, the geothermal resource prospects in the Hejin region are highly promising compared to those in the southern Yuncheng Basin.

Over the past 20 years, several geothermal boreholes have been drilled in the Hejin region; most wells have penetrated both the Cenozoic and Paleozoic sediments that overlie the Proterozoic basement. The lithological profiles derived from these borehole observations are presented in Figure 3, which also displays temperature logs (*T* logs) recorded at thermal equilibrium along these deep boreholes. Table 2 summarizes the geothermal and geological conditions collected from these geothermal wells. In the Wujiaguan village (WJG), Beiyuan village (BY), and Jinxin Community (JX) wells, the revealed reservoir rocks comprise Cambrian–Ordovician limestones and Paleogene sandstones, but the Taiyang village (TY) and Longmen Community (LM) wells

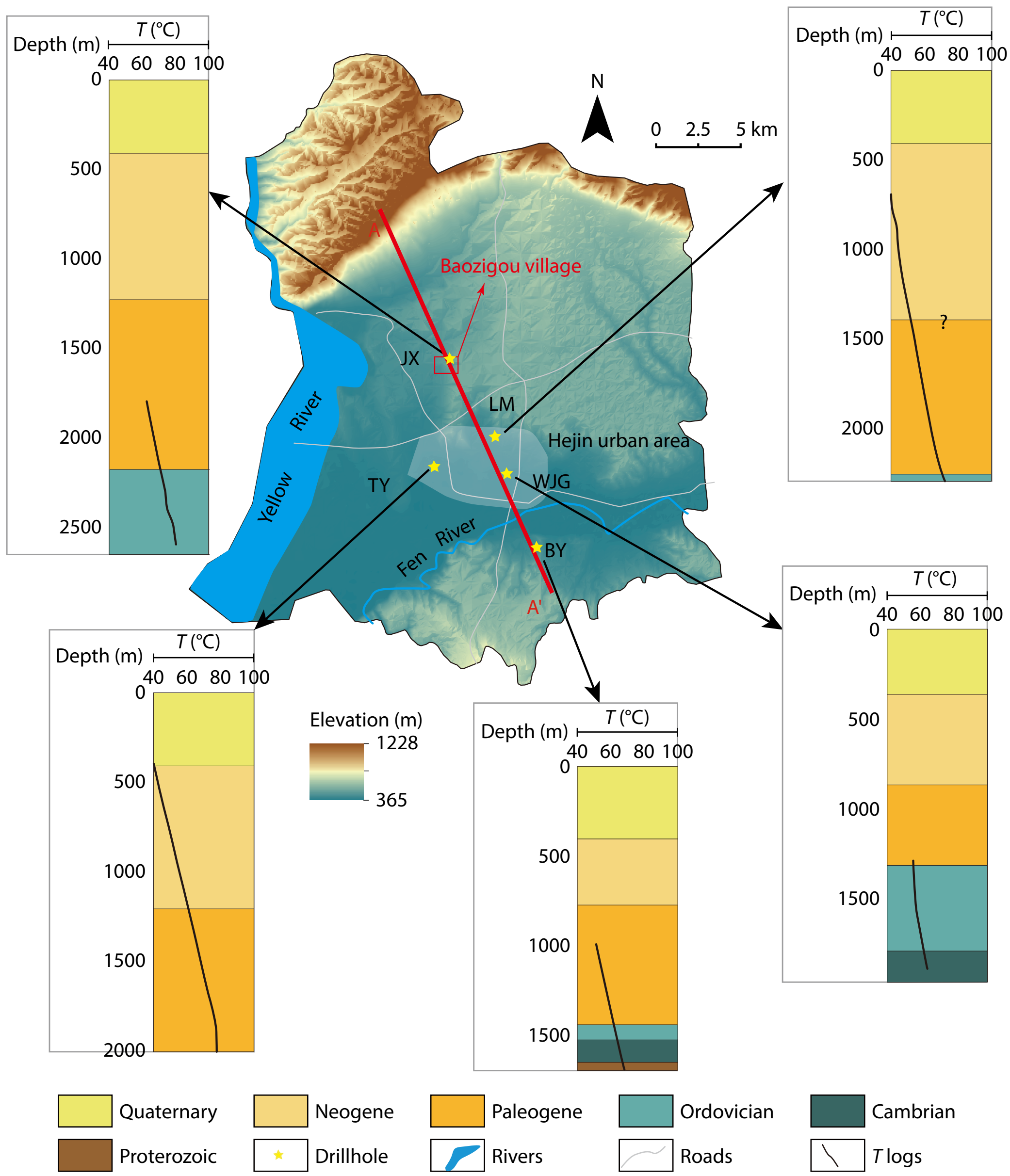

Figure 3. Simplified administrative and elevation map of the Hejin region, showing detailed lithological and temperature data from existing geothermal drill holes, and the location of Baozigou village and the AA' profile.

Table 2. Geothermal and geological conditions collected from several geothermal wells within the Hejin region.

Borehole name	Depth (m)	BHT (°C)	Average gradient (°C/100 m)	Water type	TDS (mg/L)	pH	Reservoir type
TY	2038.52	78.7	3.25	Cl-SO_4-Na	2298	8.10	Paleogene sandstones
LM	2300.00	72.8	2.07	SO_4-Cl-Na	3972	8.26	Paleogene sandstones
WJG	1976.66	63.6	2.53	Cl-SO_4-Na·Ca	1700	7.50	Cambrian–Ordovician limestones
JX	2656.00	81.9	2.29	Cl-SO_4-Na	3740	8.00	Ordovician limestones
BY	1702.03	68.7	3.25	Cl-SO_4-Na	1208	7.50	Cambrian–Ordovician limestones

contain Paleogene sandstones only. The highest BHT recorded is in the JX borehole –81.9 °C at a depth of 2613.0 m. The *T* logs indicate an average geothermal gradient of 2.53 °C/100 m in the WJG borehole, 3.25 °C/100 m in the TY borehole, 3.25 °C/100 m in the BY borehole, 2.29 °C/100 m in the JX borehole, and 2.07 °C/100 m in the LM borehole. *T* logs obtained from these wells indicate that temperature increases almost linearly with depth and is mostly not influenced by hydrothermal convection associated with faults. Table 2 also lists the primary hydrochemistry characteristics of thermal water from the five boreholes drilled in the Hejin region.

Total Dissolved Solids (TDS) range from 1208 mg/L to 3972 mg/L, indicating a relatively high concentration of major ions. The pH levels measured in these wells are weakly alkaline, ranging between 7.50 and 8.26; predominant chemical compositions are Cl-SO_4-Na-Ca and Cl-SO_4-Na water types.

The study area, Baozigou village, is situated approximately 5 km northeast of the Hejin urban area, at an elevation of 400 m above mean sea level (MSL). The JX borehole is located to the north of Baozigou village. As an important industrial area, the Hejin region faces some significant environmental challenges and pollution problems. Over the past five years, Baozigou village has undertaken a major initiative by implementing a large, centralized heating system that utilizes ground-source heat pump systems to effectively address heating needs while reducing associated air pollution problems. Small, moderate- and low-temperature geothermal projects for rural electrification and heating are quite cost-effective and capable of meeting energy demands (Chandrasekharam and Jochen, 2008). Hence, the advancement of deep geothermal prospecting is expected to further enhance the utilization of clean energy in the village. The specific objective of this project is to investigate the potential presence of high-temperature, water-bearing structures within the carbonate reservoir located beneath the Baozigou village.

3. Methods

3.1 CSAMT Investigation

The CSAMT method is an electromagnetic-sounding technique that employs a finite-length grounded electric dipole as its field source. As shown in Figure 4a, this method involves the simultaneous observation of electrical and magnetic field parameters at a specified distance from the dipole center (Susilawati and Mustopa, 2019). Specifically, the electric fields ($\boldsymbol{E}_x$) are measured using pairs of electrodes aligned parallel to the source dipole, while the perpendicular magnetic fields ($\boldsymbol{H}_y$) are measured with coils. The apparent resistivity and phase values are then derived from the impedance, defined as the ratio of $\boldsymbol{E}_x$ to $\boldsymbol{H}_y$,

$$\boldsymbol{Z}_{xy} = \frac{\boldsymbol{E}_x}{\boldsymbol{H}_y}, \tag{1}$$

$$\rho_a = \frac{1}{2\pi\mu \cdot f}\left|\boldsymbol{Z}_{xy}\right|^2, \tag{2}$$

$$\varnothing_a = \tan^{-1}\left(\frac{\mathrm{Im}\left(\boldsymbol{Z}_{xy}\right)}{\mathrm{Re}\left(\boldsymbol{Z}_{xy}\right)}\right), \tag{3}$$

where, $\boldsymbol{Z}_{xy}$ is impedance, ρ_a is the apparent resistivity, $\varnothing_a$ is the phase angle. 2-D inversion techniques were applied from the combination of the apparent resistivity and phase values to obtain reliable resistivity-depth sections. The CSAMT is particularly effective in identifying low resistivity anomalies typically associated with faults and/or altered hydrothermal minerals, making it very suitable for geothermal exploration (Hu XY et al., 2013; Yang Y et al., 2023; Basaloom and Hassan, 2025).

These CSAMT measurements in the operating frequency range of 0.125 Hz to 8192 Hz were carried out during August 2022 (Figure 4b). In this survey, the transmitter and receiver utilized are the high-power GGT-30 and the multifunctional GDP-32, respectively, both produced by Zonge International Company. The distance between the transmitting poles AB is 1 km, while the distance between the receiver poles MN is 50 m. The distance between the

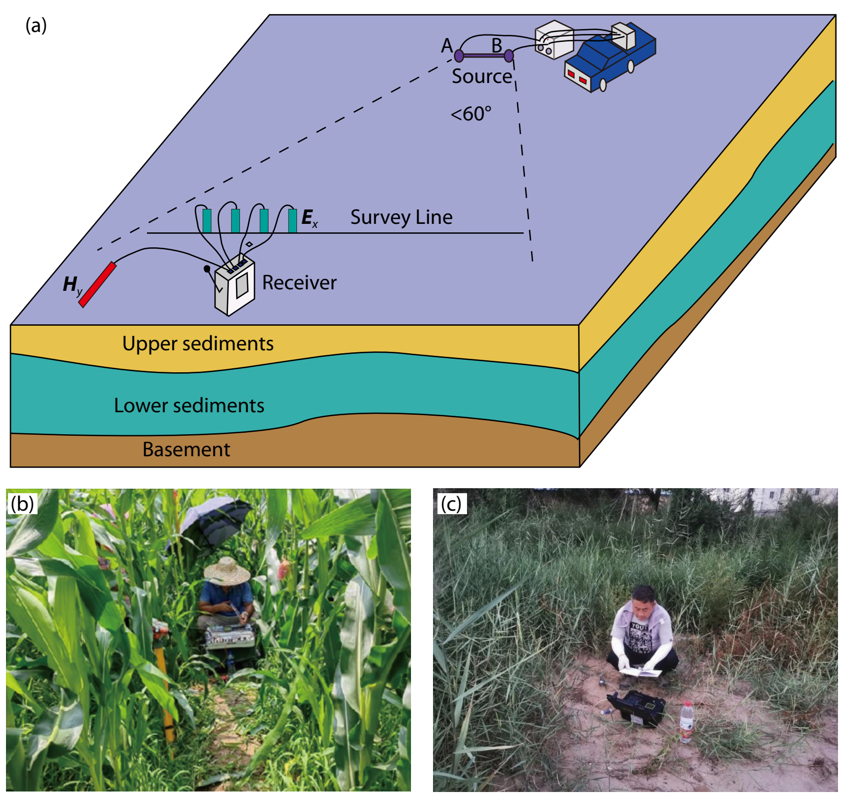

Figure 4. Schematic diagram and fieldwork. (a) Schematic diagram of the field operation mode of the CSAMT method; the fieldwork on CSAMT (b) and radon (c) measurement in Baozigou village.

transmitter and receiver ranges from 8 km to 11 km, which is sufficient for conducting measurements in far- and intermediate-field zones due to the low resistivity at shallow depths. The emission angle of the transmitter is configured to be less than 60°, which enhances the propagation of electromagnetic waves underground, minimizes reflection losses, and consequently improves detection effectiveness. As the CSAMT profiles were conducted in proximity to the nearby villages, we were alert to the possibility that the useful signals might encounter interference from surrounding ambient cultural and industrial noise. To enhance the signal-to-noise ratio, we implemented several strategies, including amplifying the transmitter power supply signal and increasing the number of iterations. Those configurations are designed to acquire resistivity data from the surface down to a depth of approximately 3 km, effectively meeting the survey objective.

The primary structural orientation within the Yuncheng Basin is predominantly northeast (NE), with some minor structures oriented northwest (NW). However, the specific structural orientation beneath Baozigou village remains unclear. To address this uncertainty, we designed a series of approximate north–south and east–west measurement profiles to ensure that at least one profile direction would intersect with the main structural orientations (NE or NW), thereby capturing all potentially significant structures at depth. Figure 5 shows the six CSAMT array profiles, named K01, K02, K03, K04, K05, and K06, with lengths of 1.0 km, 1.3 km, 1.8 km, 1.5 km, 1.4 km, and 1.05 km, respectively. K01, K02, and K03 follow an approximately east–west orientation; the remaining three profiles, K04, K05, and K06, are aligned nearly north–south. These six profiles distribute 160 CSAMT receivers along a total of 8.05 km. In addition, the obvious layering of the stratum beneath the receivers facilitates application of the relatively cost-effective scalar mode observation. Note that the JX drill hole is situated near the north-end profile of K06 in the study area.

In the data processing, we applied the Hanning window spatial filter method to mitigate the static effect resulting from the lateral non-uniformity of the near-surface electrical conductivity (Torres-Verdín and Bostick, 1992). The apparent resistivity and impedance phase data from all six CSAMT profiles were processed using the SCS2D inversion program (Scott and Mykle, 2001). This program, developed by Zonge International Company, employs a two-dimensional finite-element algorithm originally developed for natural-source magnetotelluric (MT) data (deGroot-Hedlin and Constable, 1990; Cheng YZ et al., 2023). The transverse magnetic (TM-mode) data are inverted. The initial model for the 2D inversion comprises a smooth version of the apparent resistivity, incorporating CSAMT station locations and Bostick depths (Jones, 1983).

3.2 Radon Measurement in Soil

Radon (^{222}Rn, half-life 3.84 days) is a naturally occurring radioactive inert gas produced through the radioactive decay series of ^{238}U (Fleischer and Mogro-Campero, 1978; Bonotto and Santos, 2007). Although uranium is found in almost all rocks, it is particularly enriched in silica-rich rocks such as granites, gneisses, schists, volcanics, pegmatites, and migmatites. To be released to the surface, radon, due to its limited mobility, requires a transporting agent such as hot water or other fluids along the fractured zone or faults in geothermal fields (Aydar and Diker, 2021). Seyis et al. (2010) further observed that sites with high geothermal activity contain much higher levels of radon in the soil compared to sites with low or no geothermal activity. Radon measurements are both time-efficient and cost-effective. Additionally, they are not affected by electrical or magnetic interference. Nowadays, mapping radon concentrations and radon flux anomalies has been proposed as an effective way of detecting buried or hidden

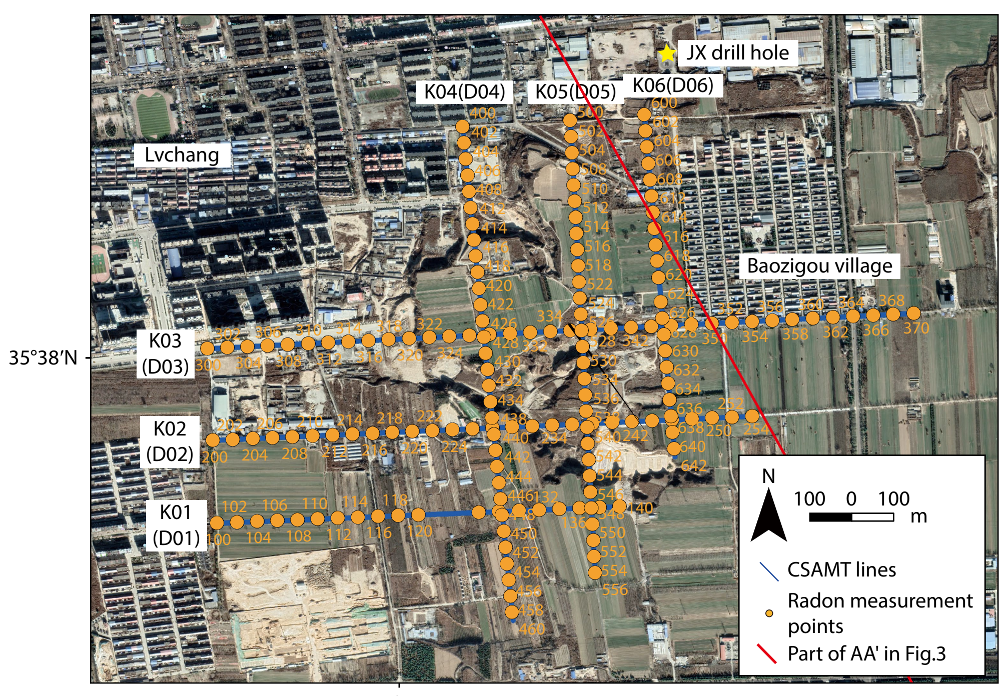

Figure 5. Location map of CSAMT and radon measurement surveys in Baozigou village.

faults (Burton et al., 2004; Seyis et al., 2010; Neri et al., 2016; Afero et al., 2024).

We measured radon concentrations in soil gas in alignment with the abovementioned CSAMT profiles (see Figure 5), thereby facilitating comprehensive interpretation and mutual validation. As shown in Figure 4c, radon sampling in the study area was conducted at depths between 0.6 m and 0.8 m using a steel soil probe attached to an FD216 radon detector developed by the Beijing Research Institute of Uranium Geology (Li JB et al., 2022). Radon concentrations were recorded at 11-minute intervals. Sampling points were spaced approximately 50 m apart, corresponding to the distance between CSAMT receivers. A total of 167 measurement points were distributed across six lines, labeled D01 through D06, as detailed in Figure 5. To mitigate the potential influence of rainfall, radon soil gas sampling was postponed for about 24 hours when it rained. Quality control measures were implemented to ensure the accuracy and reliability of the field measurements. We performed statistical analyses of soil gas radon concentrations, including the mean ($\bar{X}$), and standard deviation (σ). Measurements falling outside the range ($\bar{X}-3\sigma, \bar{X}+3\sigma$) were discarded. The mean value is designated as the *radon background value* (RnB). The sum ($\bar{X}+\sigma$) between the RnB and the standard deviation constitutes the *radon threshold value* (RnT). Measurements exceeding the RnT value are considered significant radon anomalies.

4. Results

4.1 CSAMT Resistivity Structures

The CSAMT resistivity structures in Baozigou village could be well constrained by the nearby Jinxin borehole in the north of the study area, as well as by regional petrophysical resistivity studies (Table 1). Generally speaking, the subsurface resistivity structures in the study area reflect the characteristic lithology and/or tectonics, as well as potential groundwater and/or hydrothermal alteration. Figures 6 and 7 illustrate the inversion results and the associated geological interpretations from CSAMT profiles.

Figures 6a, 6b, and 6c present the subsurface resistivity structures along the three parallel east–west trending profiles (K01, K02, and K03); they exhibit quite similar characteristics, and all vary predominantly vertically. These resistivity profiles exhibit sub-horizontal stratification, characterized by alternating high-low-high resistivity values from the surface to deeper formations. The uppermost high-resistivity layers, corresponding to loose Quaternary clastic, encapsulate some low-resistivity anomalous traps. The thickness of the Quaternary layer ranges from approximately 300 m to 400 m, with resistivity values mostly higher than 80 Ωm. The underlying region, buried at elevations ranging from 0 m to −700 m MSL, is characterized by anomalous low resistivity values of less than 20 Ωm. It is noteworthy that this low resistivity anomaly trends upward at the left side, which is particularly evident in the K02 profile. Those low resistivity anomalies are possibly associated with a small-scale fault (F_b) inclined to the left. The third layer, exhibiting higher resistivity values between 50 Ωm and 100 Ωm, is inferred to be Paleogene sandstones. This layer can extend to a maximum depth of −1800 m MSL. At greater depths, the high-resistivity layer, characterized by values exceeding 100 Ωm, is composed predominantly of Ordovician and Cambrian limestones. In addition, the resistivity contours within the Ordovician and Cambrian formations exhibit a downward

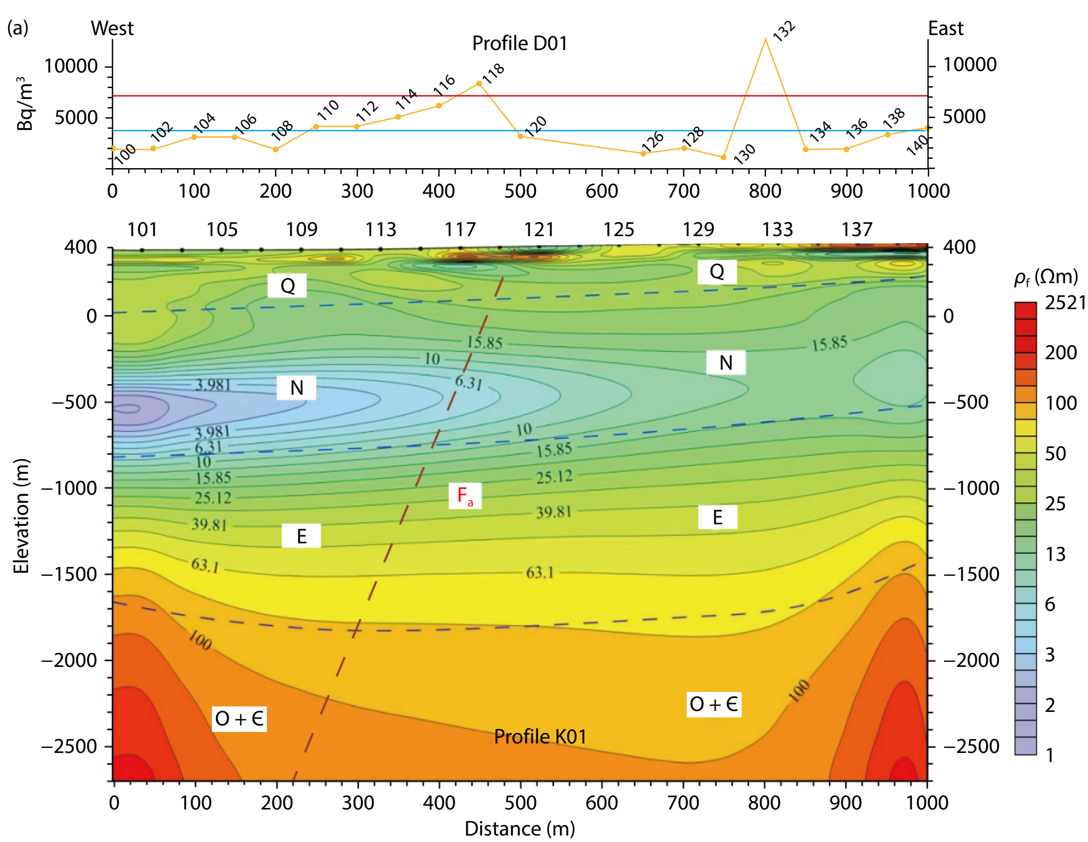

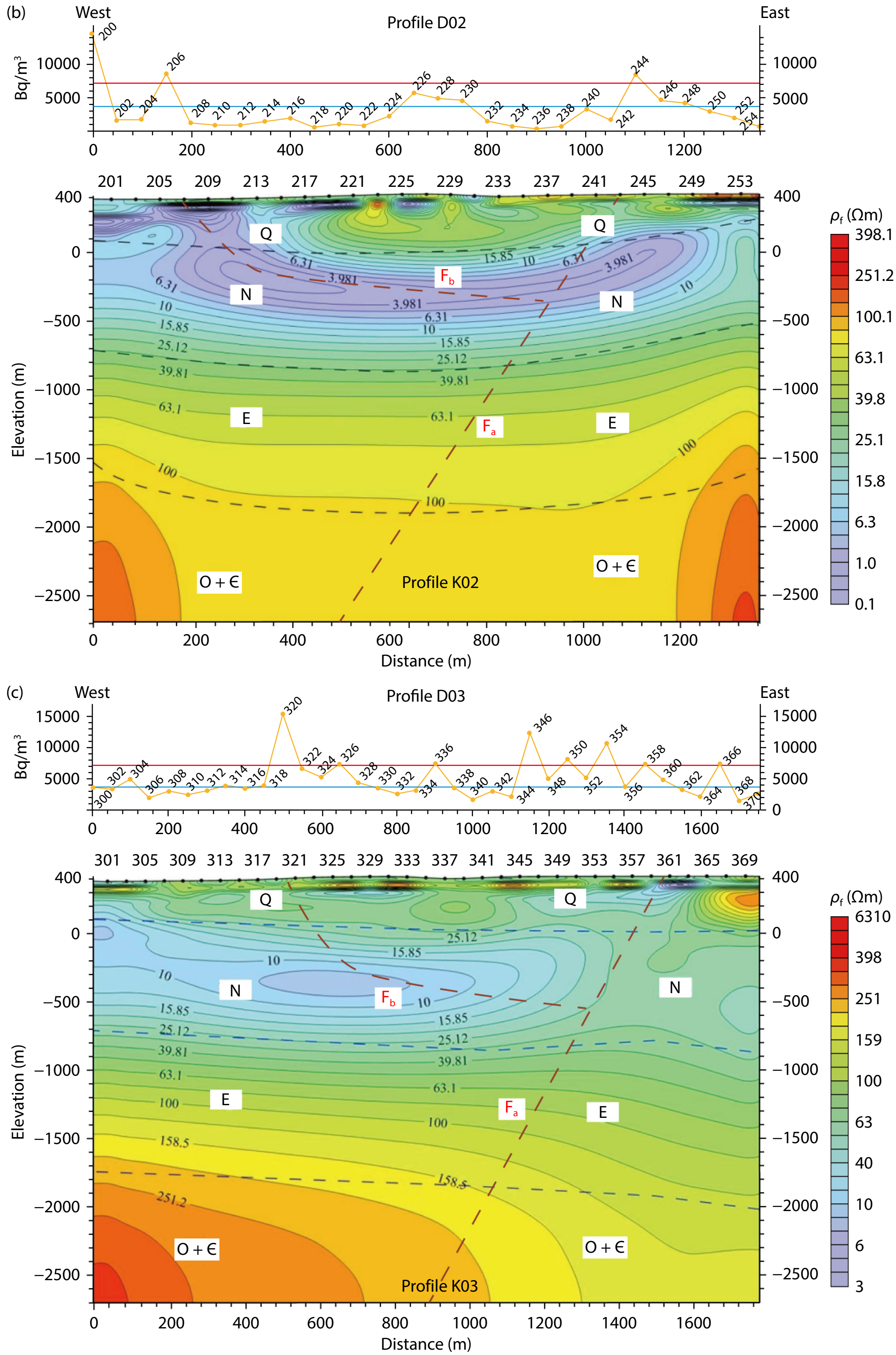

Figure 6. Resistivity sections of CSAMT profiles K01 (a), K02 (b), K03 (c), desplayed beneath each profile's the corresponding radon profile: D01 (a), D02 (b), D03 (c). Locations of the CSAMT receiver stations and radon measurement points are indicated by the numbers 100–140 (a), 200–254 (b), 300–370 (c). In the radon profiles, blue solid lines represent the RnB value; red solid lines represent the RnT value. ρ_f is apparent resistivity.

bend, possibly indicating the presence of a deep fault (F_a), which will be better revealed in the NS-trending CSAMT profiles.

In the north–south oriented K04, K05, and K06 profiles (Figures 7a, 7b, and 7c), the derived resistivity structures show considerable similarity to those observed in the previously analyzed EW-trending sections. However, a mid-to-high lateral variation in resistivity is observable across all three NS-trending profiles, which is interpreted to be caused by a normal fault. This fault, designated as F_a,

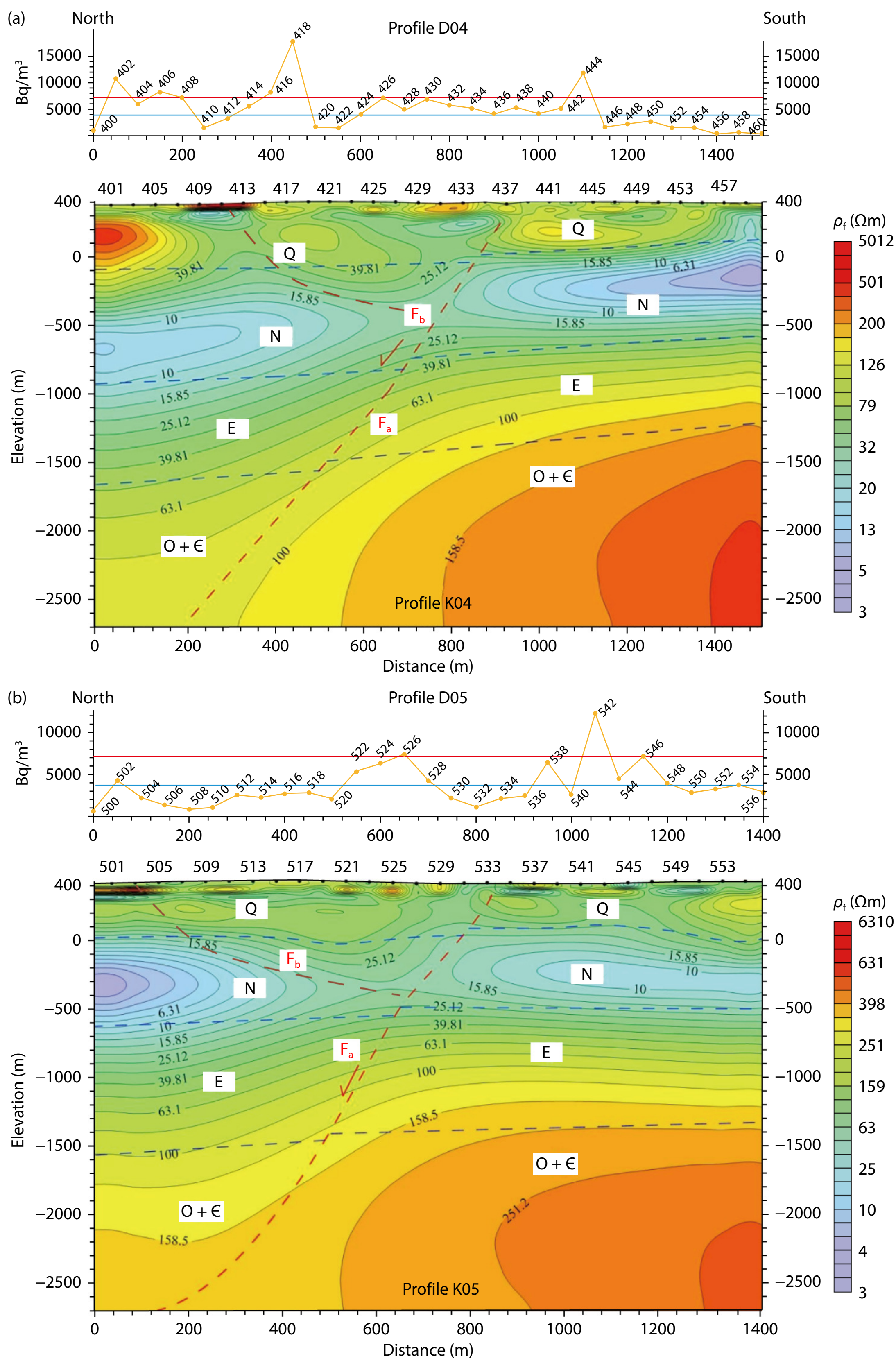

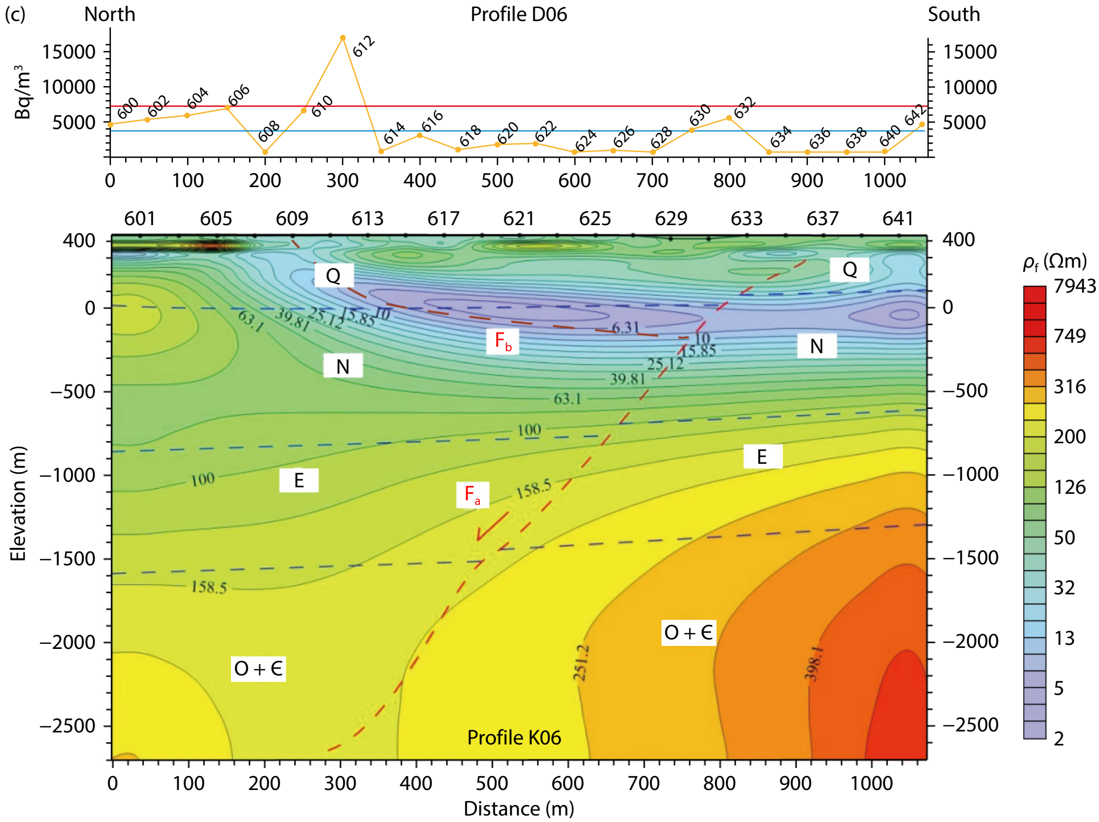

Figure 7. Resistivity sections of CSAMT profile K04 (a), K05 (b), K06 (c), along with the corresponding radon profiles D04 (a), D05 (b), D06 (c) at the top. Locations of the CSAMT receiver stations and radon measurement points are indicated by the numbers 400–460 (a), 500–556 (b), 600–642 (c). In the radon profiles, blue solid lines represent the RnB value; red solid lines represent the RnT value. ρ_f is apparent resistivity.

is characterized by a rightward inclination with obvious displacement and seems to extend from the surface to a significant depth (deeper than −2500 m MSL).

4.2 Radon Survey Results

Radon concentrations in soil along the profiles D01–D06 are given above the CSAMT resistivity structures in Figures 6 and 7. In Baozigou village, the dominant surface lithology consists of Quaternary soil or sandy soil. The measured soil gas radon concentrations vary significantly, ranging from 170.45 Bq/m^3 to 17727.27 Bq/m^3. The average radon concentration of 3899.26 Bq/m^3 indicates the substantial radon presence in the soil, likely resulting from active emanation processes associated with underlying geological structures. The standard deviation of 3221.87 Bq/m^3 highlights the spatial heterogeneity of radon concentrations, possibly reflecting variations in rock permeability and geothermal activity. Therefore, the calculated RnB and RnT values are 3899.26 Bq/m^3 and 7121.13 Bq/m^3, which are plotted in Figures 6 and 7. Measurement points with radon values exceeding the RnT are regarded as high outliers listed in Table 3. It is found that high outliers are distributed mostly near the ends of each profile, which correspond mainly to the locations of F_a and F_b extending to the surface manifestations. However, it is important to note that not all RnT outliers necessarily indicate the presence of fractured zones. Clay minerals formed during soil production and a fluctuating water table can also cause relatively high radon values (Easterbrook, 1999; Taylor and Eggleton, 2001). The high radon value at 132, for example, may be a consequence of the clay overburden at that location rather than being related to fractures beneath it.

Table 3. Observed stations with radon values larger than the radon threshold value (RnT).

Radon profiles	Observed stations larger than RnT
D01	118, 132
D02	200, 206, 244
D03	320, 346, 350, 354, 358, 366
D04	402, 418, 444
D05	526, 542, 546
D06	612

The absence of depth information in radon measurements poses a challenge in accurately determining the location, width, and depth of the anomalies related to faults (Gan FP et al., 2012). Consequently, radon results alone are insufficient to indicate the presence of fractures and need to be integrated with CSAMT resistivity profiles. As illustrated in Figure 8a, these high radon manifestations have outlined the orientation of the identified faults. from these high radon manifestations has been outlined. Integrated with CSAMT resistivity profiles, we see that F_a and F_b are both NNE-trending but have opposite dips. The application of the

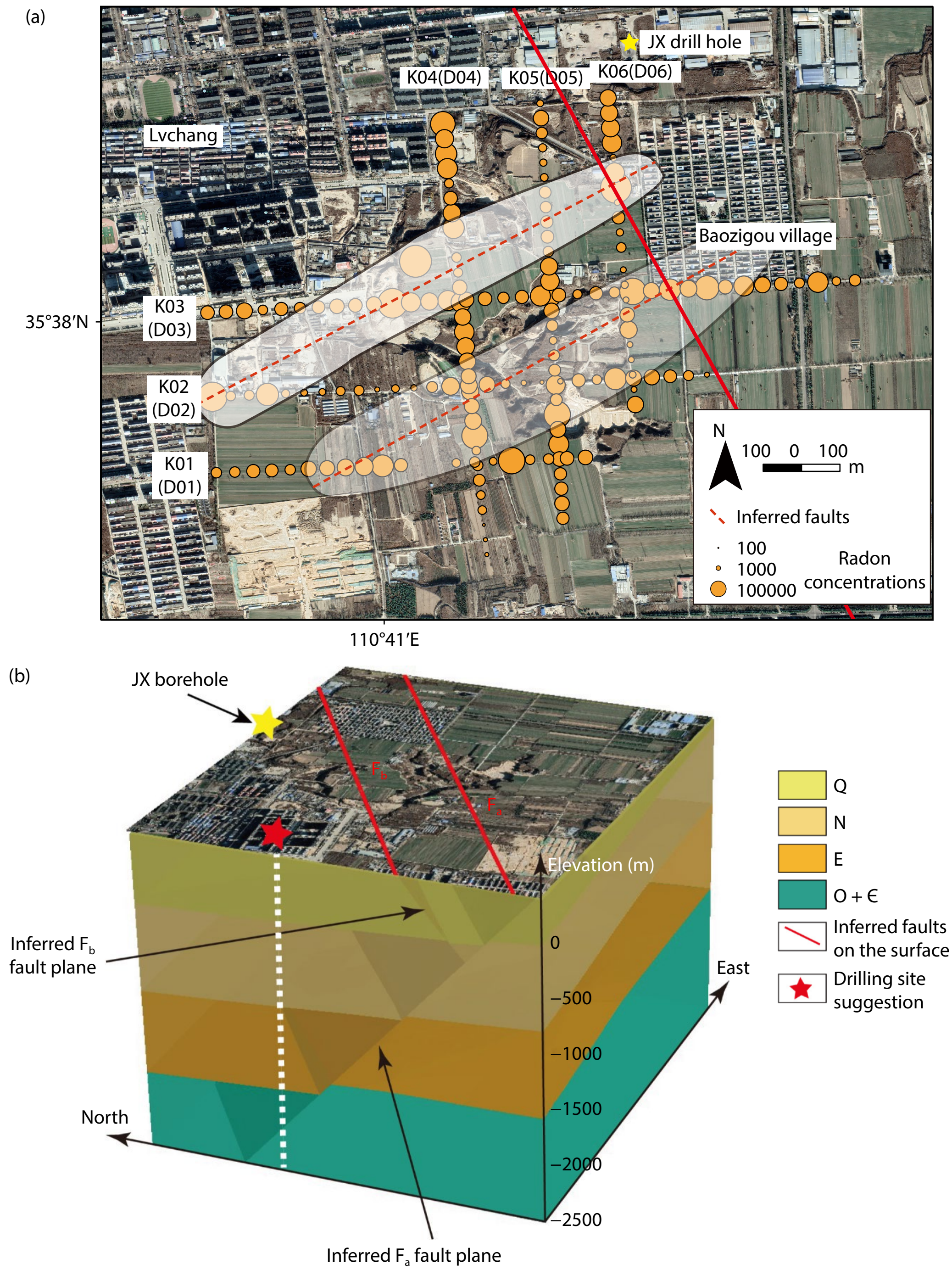

Figure 8. Interpreted surface faults and 3D geological model beneath Baozigou village (Hejin region) derived from CSAMT and radon data, (a) Surface locations of the interpreted faults; the radon concentrations are proportional to the radius of the yellow circles. (b) 3D geological model beneath Baozigou village, inferred from CSAMT and radon data interpretations.

two methodologies makes the geological and tectonic findings in this study more persuasive.

5. Discussion

5.1 Characteristics of Baozigou Village Geothermal System

The thick Quaternary overburden in the study area, along with cultivated environments such as residential areas and farmlands, prevent direct observation of underlying lithologies and potential tectonics at depth. By integrating CSAMT resistivity structures, radon measurements, and associated geological and drilling data, we present here a more convincing 3D geological model of the study area (Figure 8b). This model provides valuable insights into delineating the primary characteristics of the concealed geothermal field beneath Baozigou village, where Quaternary and Neogene clastic layers are widespread and present with thicknesses ranging from approximately 300 to 600 m, obviously acting as a clay cap for the geothermal system. Within the Quaternary layers, shallow zones with higher resistivity are likely associated with unaltered and dry rocks near the surface, whereas areas with lower resistivity (less than 20 Ωm) may indicate the presence of shallow phreatic aquifers. The underlying highly conductive anomalies primarily belong to the Neogene unit and are interpreted as being related to low-resistivity clay hydrothermal alteration. The clay mineral involved is likely smectite, which has a high cation exchange capacity (CEC) and can significantly reduce the resistivity of primary rocks (Ussher et al., 2000; Lévy et al., 2018; Hersir et al., 2020; Rizzello et al., 2021, 2022). Rocks containing smectite clays always exhibit low permeability characteristics and may also indirectly suggest intermediate temperatures (Ussher et al., 2000; Cumming, 2009). Moreover, the presence of smectite suggests highly active hydrothermal circulation. The observed increase of resistivity with depth in the Paleogene sandstones is likely attributed to a decrease in porosity as depth increases, as well as a reduction in smectite clay content, which usually becomes unstable at temperatures over 70 °C (Gunderson et al., 2000). The underlying layer with much higher resistivity is inferred to be deep resistive limestone formations. Overall, the Quaternary and Neogene clastic formations serve as the geothermal cap, while the Paleogene sandstones, along with the Lower Ordovician and Cambrian limestones, constitute the geothermal reservoirs beneath Baozigou village. The base of the reservoirs is likely marked by the impermeable Proterozoic metamorphic rocks at unknown depths, which are not shown in resistivity profiles.

Both identified Baozigou faults, F_a and F_b, exhibit normal fault characteristics and are oriented in an NEE direction (approximately 255°) and run roughly parallel to the western Hejin segment of F1, suggesting that these newly identified faults may be secondary faults associated with F1. Enhanced permeability along faults F_a and F_b may facilitate hydraulic connectivity between the upper and deep lower geological strata, potentially promoting the formation of fractured (damaged) zones with high permeability associated with hydrothermal geothermal fields. Specifically, the high-angle deep normal fault F_a dips at 70° with a displacement of about 100 m, and cuts through nearly all subsurface sequences, suggesting it may play a more significant role in promoting hydraulic and thermal convection. In contrast, fault F_b is mainly confined to the Cenozoic strata and does not penetrate the basement rocks at depth.

5.2 Geothermal Conceptual Model of the Hejin Region

A conceptual model is particularly effective when exploring blind prospects because it makes fuller use of limited data and helps identify strategies to address the lack of information, as well as identifying targets (Cumming, 2009). Because of a lack of relevant data, no geothermal model had been proposed for the Fenwei Depression within the Yuncheng Basin prior to this paper. Figure 9 illustrates our preliminary two-dimensional conceptual model along the NW-trending AA' profile in Figure 2. We have constructed this 2D geothermal conceptual model, orthogonal to the main NE-trending faults within the Yuncheng Graben, based on all available geological data (e.g., surface geological maps, borehole logs from the Hejin Graben), geophysical measurements (e.g., CSAMT, regional magnetic and gravity data), and associated geochemical results that are relevant to geothermal exploration and development activities.

Just like Yanggao–Tianzhen and Xianyang–Xi'an geothermal fields within the Fenwei Rift, the main heat source in our model is conduction from the uplifted mantle beneath the significantly thinned lithosphere to the surface (Zhou WL et al., 2020; Cai Y et al., 2021). Additionally, a low-velocity and high-conductivity layer in the deep crust, identified through MT and seismic surveys (Xing ZY et al., 2005), could be linked to thermal anomalies at depth. The possible Mesozoic granitic intrusions at depth, always characterized by their relatively high thermal conductivity, tend to be good heat conductors rather than heat sources, as they likely intruded during the Cretaceous and have since cooled down. The reservoirs in the Fen River Depression are composed primarily of sub-horizontal and/or horizontal carbonate and sandstone layers, while the Quaternary and/or Neogene sedimentary cover serves as the cap rocks. The geothermal fluids at depth originate mainly from precipitation, which is indicated by the hydrogeochemistry study from the eastern Xinjiang geothermal field (Chen Y, 2023). Faults significantly influence the circulation of fluid within such blind geothermal systems. The deeply penetrating F1 and F2, acting as geothermal fluid pathways, could channel cold meteoric water to substantial depth in the middle part of Hejin Depression (i.e., beneath the Fen River). Some shallow groundwater recharge also occurs via seepage from the surface Fen River. The hydraulic gradient between the Lüliang mountain/Emei uplift and the Fen River valley drives the water flow through highly porous and permeable sedimentary reservoirs at depth, increasing the water's temperature as it travels. Despite no observed geothermal manifestation on the surface, the heated water at depth may rise buoyantly to shallower reservoirs and/or may emerge along high-permeable faults in the central part of the Fen River Depression, such as the F_a identified in the Baozigou area. We also suggest that the deep groundwater beneath the central part is subjected to more intensive water–rock interactions and is far from cold water supply areas, which is verified by the chemical composition of geothermal water samples and high TDS in Table 2. Therefore, some large-scale tectonic fractures and faults with increased permeability in the central segments of the Fen River Depression, which may act as up-flow zones for geothermal fluids, represent promising geothermal targets and require further investigation.

5.3 Geothermal Drilling Site Suggestion

Drilling a geothermal well represents the most critical phase of geothermal development, owing to the substantial investment risk, relative to the costs of all other investigative studies and field surveys, including geology, geochemistry, and geophysics. Nevertheless, identifying convection zones—the most efficient mechanism of energy transfer within the Earth—through drilling can serve as an effective tool for exploring prospective geothermal reservoirs (Boden, 2016). Common targets for well sites within a reservoir include permeable formations, contact zones between different lithologies, and faults and fractures, where thermal convection consistently occurs (Zarrouk and McLean, 2019; Zhang YQ et al., 2024). Notably, geothermal fluids that ascend within fault zones result in more elevated temperatures and significantly steeper thermal gradients than are achievable by conduction alone.

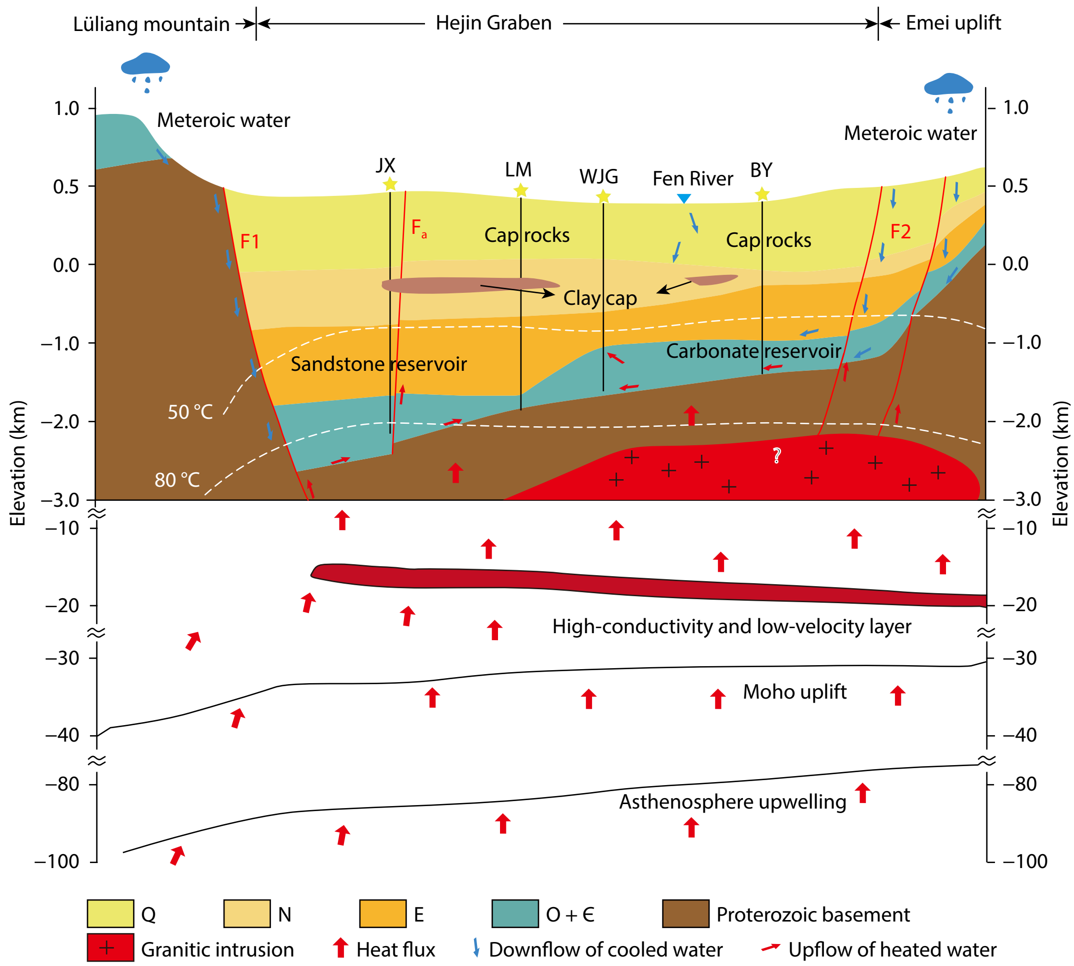

Figure 9. Preliminary two-dimensional geothermal conceptual model in the Fen River Depression along the AA' profile.

Based on the conceptual model we have constructed, and our interpretation of CSAMT and radon data, we suggest that the newly identified deep normal fault F_a is likely to facilitate fluid circulation and thermal convection at great depth. Additionally, the resistivity values of the deep carbonates on the northwestern side of the F_a fault are lower than those on the southeastern side, which suggests that the deep carbonate aquifer within the hanging wall of F_a may contain more geothermal water. In addition, another relatively small-scale fault, F_b, is found in the northwestern part of the study area. Therefore, drilling within the hanging wall block of the identified normal fault F_a is strongly recommended. As illustrated in Figure 2, the temperature profile in the JX borehole increases linearly with depth, which indicates that it doesn't encounter the thermal water upflows typically associated with fault zones at depth. However, drilling close to fault zones F_a and F_b can enhance the likelihood of encountering elevated geothermal anomalies due to fluid circulation. If the future drill work is restricted to be within the study area, we propose drilling a geothermal well in the northwest of the study area, to a total depth of at least 2300 m; that location is denoted as a red star in Figure 8b. This borehole would possibly penetrate the potentially fractured Ordovician carbonates at depth, thereby ensuring a substantial volume of geothermal water with higher temperatures.

6. Conclusion

This research employed both the highly anti-interference CSAMT and radon methods to investigate the subsurface lithology and structures associated with the geothermal system in Baozigou village, Yuncheng Basin, Fenwei Rift, China. The results of CSAMT and radon surveys revealed the distribution of the subsurface lithology and structures, aiding in identification of potential geothermal drilling sites when integrated with a constructed geothermal conceptual model. The main findings can be summarized as follows:

(1) CSAMT profiles effectively delineated the subsurface resistivity structures, enabling the mapping of key geological features, particularly two faults. These two faults are spatially correlated with elevated radon concentrations in radon profiles. Those two faults exhibit normal characteristics with opposite dips and are inferred to be secondary faults of the Lüliang mountain fault. By integrating the CSAMT interpretation results and regional geological understanding, a three-dimensional subsurface geological model beneath Baozigou village was further constructed.

(2) Based on the available geological, geophysical, and geochemical data, including the CSAMT and radon results, a geothermal conceptual model for the Fen River Depression was developed. This model elucidates critical aspects of the geothermal system within the Fen River Depression, including the heat source,

geothermal reserves, and fluid dynamics within the inflow and outflow zones, which indicates that the permeable fault zones in the central part of the Fen River Depression have great geothermal potential.

(3) All these analyses give insights into potential targets for geothermal drilling. Consequently, a site in the northwest of the Baozigou village has been recommended for deep geothermal drilling to intersect the carbonate reservoir and associated water-conducting fault structures at depth.

Acknowledgments

This research was jointly supported by the Shanxi Province Basic Research Program (No. 20210302123374), Yuncheng University Doctoral Research Initiation Fund (No. YQ-2021008), Excellent doctors come to Shanxi to reward scientific research projects (No. QZX-2023020), Open Fund of State Key Laboratory of Precision Geodesy (No. SKLPG2025-1-1), Joint Open Fund of the Research Platforms of School of Computer Science, China University of Geosciences, Wuhan (No. PTLH2024-B-03), and Hubei Provincial Natural Science Foundation Project (No. 2025AFC095).

References

Afero, F., Dear, V., and Husin, A. (2024). The investigation of the dominant direction of the fault structure using the radon method at Mt. Pancar geothermal field. *J. Geosci. Eng. Environ. Technol.*, *9*(1), 52–57. https://doi.org/10.25299/jgeet.2024.9.1.14556

Armadillo, E., Rizzello, D., Pasqua, C., Pisani, P., Ghirotto, A., Kabaka, K., Mnjokava, T., Mwano, J., Didas, M., and Tumbu, L. (2020). Geophysical constraints on the Luhoi (Tanzania) geothermal conceptual model. *Geothermics*, *87*, 101875. https://doi.org/10.1016/j.geothermics.2020.101875

Aydar, E., and Diker, C. (2021). Carcinogen soil radon enrichment in a geothermal area: Case of Güzelçamlı-Davutlar district of Aydın city, western Turkey. *Ecotoxicol. Environ. Saf.*, *208*, 111466. https://doi.org/10.1016/j.ecoenv.2020.111466

Aykaç, S., Timur, E., Sari, C., and Çaylak, Ç. (2015). CSAMT investigations of the Caferbeyli (Manisa/Turkey) geothermal area. *J. Earth Syst. Sci.*, *124*(1), 149–159. https://doi.org/10.1007/s12040-014-0521-1

Basaloom, A., and Alzahrani, H. (2025). Application of controlled-source audio-frequency magnetotellurics (CSAMT) for subsurface structural characterization of Wadi Rum, Southwest Jordan. *Sustainability*, *17*(5), 2107. https://doi.org/10.3390/su17052107

Baubron, J. C., Rigo, A., and Toutain, J. P. (2002). Soil gas profiles as a tool to characterise active tectonic areas: the Jaut Pass example (Pyrenees, France). *Earth Planet. Sci. Lett.*, *196*(1-2), 69–81. https://doi.org/10.1016/S0012-821X(01)00596-9

Boden, D. R. (2016). *Geologic Fundamentals of Geothermal Energy*. Boca Raton: CRC Press. https://doi.org/10.1201/9781315371436

Bolinger, M., Millstein, D., Gorman, W., Dobson, P., and Jeong, S. (2023). Mind the gap: Comparing the net value of geothermal, wind, solar, and solar+storage in the Western United States. *Renew. Energy*, *205*, 999–1009. https://doi.org/10.1016/j.renene.2023.02.023

Bonotto, D. M., and Santos, T. O. (2007). Health risk related to radon in a thermal SPA utilizing waters from Guarani aquifer. In: C. A. Brebbia (Ed.), *Environmental Health Risk IV* (pp. 137–146). Southampton: WIT Press. https://doi.org/10.2495/EHR070151

Burton, M., Neri, M., and Condarelli, D. (2004). High spatial resolution radon measurements reveal hidden active faults on Mt. Etna. *Geophys. Res. Lett.*, *31*(7), L07618. https://doi.org/10.1029/2003GL019181

Cai, Y., Wu, J. P., Rietbrock, A., Wang, W. L., Fang, L. H., Yi, S. and Liu, J. (2021). *S* wave velocity structure of the crust and upper mantle beneath Shanxi rift, central North China Craton and its tectonic implications. *Tectonics*, *40*(4), e2020TC006239. https://doi.org/10.1029/2020TC006239

Chandrasekharam, D., and Bundschuh, J. (2008). *Low-Enthalpy Geothermal Resources for Power Generation*. London: CRC Press. https://doi.org/10.1201/9780203894552

Chen, L., Cheng, C., and Wei, Z. G. (2009). Seismic evidence for significant lateral variations in lithospheric thickness beneath the central and western North China Craton. *Earth Planet. Sci. Lett.*, *286*(1-2), 171–183. https://doi.org/10.1016/j.epsl.2009.06.022

Chen, Y. (2023). Chemical and isotopic characteristics of geothermal fluids in Beichi area, Xinjiang County, Yuncheng City. *HuaBeiNat. Resour. (in Chinese)*, (3), 60–62.

Chen, Y. F., Chen, J. H., Li, S. C., Yu, Z. Y., Liu, X. Z., and Shen, X. Z. (2021). Variations of crustal thickness and average Vp/Vs ratio beneath the Shanxi Rift, North China, from receiver functions. *Earth Planets Space*, *73*(1), 200. https://doi.org/10.1186/s40623-021-01528-8

Cheng, Y. Z., Wang, C., Da, W. W., Kong, Y. L., and Hu, X. Y. (2023). Anatomy of the convective geothermal system from geophysical and hydrochemical data: A case study from the Changshou geothermal field, South China. *Geophysics*, *88*(5), WB1–WB10. https://doi.org/10.1190/geo2022-0409.1

Cumming, W. (2009). Geothermal resource conceptual models using surface exploration data. In *Proceedings, Thirty-Fourth Workshop on Geothermal Reservoir Engineering* (pp. 1–6). Stanford, California.

Davidson, J. R. J., Fairley, J., Nicol, A., Gravley, D., and Ring, U. (2016). The origin of radon anomalies along normal faults in an active rift and geothermal area. *Geosphere*, *12*(5), 1656–1669. https://doi.org/10.1130/GES01321.1

deGroot-Hedlin, C., and Constable, S. (1990). Occam's inversion to generate smooth, two-dimensional models from magnetotelluric data. *Geophysics*, *55*(12), 1613–1624. https://doi.org/10.1190/1.1442813

Didas, M. M., Armadillo, E., Hersir, G. P., Cumming, W., Rizzello, D., Benediktsdóttir, Á., and Geirsson, H. (2024). New MT surveys and 3D resistivity imaging beneath the Ngozi-Rungwe volcanoes at the triple rift junction of the East African Rift System in SW Tanzania: Support for integrated interpretations of geothermal conceptual models. *Geothermics*, *118*, 102893. https://doi.org/10.1016/j.geothermics.2023.102893

Easterbrook, D. J. (1999). *Surface Processes and Landforms* (2nd ed). Upper Saddle River, New Jersey: Prentice Hall.

Erlingsson, T., Jóhannesson, T., Olafsson, E., and Axelsson, G. (2010). Geothermal district heating system in Xianyang, Shaanxi, China. In *Proceedings World Geothermal Congress* (pp. 25–29).

Fleischer, R. L., and Mogro-Campero, A. (1978). Mapping of integrated radon emanation for detection of long-distance migration of gases within the Earth: Techniques and principles. *J. Geophys. Res.: Solid Earth*, *83*(B7), 3539–3549. https://doi.org/10.1029/JB083iB07p03539

Gan, F. P., Lü, Y., Yu, L. P., and Chen, Y. X. (2012). The utilization of combined radon and CSAMT methods to detect underground geological structures: a case study of detection in Palian and Fapa profiles, Luxi area, western Yunnan Province. *Geol. Bull. China (in Chinese)*, *31*(2-3), 389–395. https://doi.org/10.3969/j.issn.1671-2552.2012.02.024

Gao, G. M., Kang, G. F., Li, G. Q., and Bai, C. H. (2015). Crustal magnetic anomaly in the Ordos region and its tectonic implications. *J. Asian Earth Sci.*, *109*, 63–73. https://doi.org/10.1016/j.jseaes.2015.04.033

Georgsson, L. S. (2009). Geophysical methods used in geothermal exploration. In *Presented at Short Course IV on Exploration for Geothermal Resources* (pp. 1–16). Lake Naivasha, Kenya: Kenya Electricity Generating Co., Ltd.

Gunderson, R., Cumming, W., Astra, D., and Harvey, C. (2000). Analysis of smectite clays in geothermal drill cuttings by the methylene blue method: for well site geothermometry and resistivity sounding correlation. In *Proceedings World Geothermal Congress* (pp. 1175–1181). Kyushu-Tohoku, Japan.

He, L. F., Chen, L., Dorji, Xi, X. L., Zhao, X. F., Chen, R. J., and Yao, H. C. (2016). Mapping the geothermal system using AMT and MT in the Mapamyum (QP) field, Lake Manasarovar, Southwestern Tibet. *Energies*, *9*(10), 855. https://doi.org/10.3390/en9100855

He, L. P., Guo, Z., Chen, Y. J., Huang, Q. H., and Yang, Y. J. (2021). Seismic imaging of a magma chamber and melt recharge of the dormant Datong volcanoes. *Earth Space Sci.*, *8*(12), e2021EA001931. https://doi.org/10.1029/2021EA001931

Hersir, G. P., Árnason, K., Vilhjálmsson, A. M., Saemundsson, K., Ágústsdóttir, Þ., and Friðleifsson, G. Ó. (2020). Krýsuvík high temperature geothermal area in SW Iceland: Geological setting and 3D inversion of magnetotelluric (MT) resistivity data. *J. Volcanol. Geoth. Res.*, *391*, 106500. https://doi.org/10.1016/j.jvolgeores.2018.11.021

Hu, X. Y., Peng, R. H., Wu, G. J., Wang, W. P., Huo, G. P., and Han, B. (2013). Mineral exploration using CSAMT data: Application to Longmen region metallogenic belt, Guangdong Province, China. *Geophysics*, *78*(3), B111–B119. https://doi.org/10.1190/geo2012-0115.1

Jolie, E., Scott, S., Faulds, J., Chambefort, I., Axelsson, G., Gutiérrez-Negrín, L. C., Regenspurg, S., Ziegler, M., Ayling, B., … Zemedkun, M. T. (2021). Geological controls on geothermal resources for power generation. *Nat. Rev. Earth Environ.*, *2*(5), 324–339. https://doi.org/10.1038/s43017-021-00154-y

Jones, A. G. (1983). On the equivalence of the "Niblett" and "Bostick" transformations in the magnetotelluric method. *J. Geophys.*, *53*(1), 72–73.

Ke, T. T., Huang, S. P., Xu, W., and Li, X. X. (2021). Study on heat extraction performance of multiple-doublet system in Hot Sedimentary Aquifers: Case study from the Xianyang geothermal field, Northwest China. *Geothermics*, *94*, 102131. https://doi.org/10.1016/j.geothermics.2021.102131

Kong, Y. L., Pang, Z. H., Shao, H. B., Hu, S. B., and Kolditz, O. (2014). Recent studies on hydrothermal systems in China: a review. *Geotherm. Energy*, *2*, 19. https://doi.org/10.1186/s40517-014-0019-8

Lévy, L., Gibert, B., Sigmundsson, F., Flóvenz, Ó. G., Hersir, G. P., Briole, P., and Pezard, P. A. (2018). The role of smectites in the electrical conductivity of active hydrothermal systems: electrical properties of core samples from Krafla volcano, Iceland. *Geophys. J. Int.*, *215*(3), 1558–1582. https://doi.org/10.1093/gji/ggy342

Li, J. B., Zhou, Z. C., Yun, L., Su, R., and Guo, Y. H. (2022). Identification of hidden faults based on soil radon measurement in the southern margin of the Beishan area, Gansu Province. *Acta Geol. Sin. (in Chinese)*, *96*(6), 2240–2250. https://doi.org/10.19762/j.cnki.dizhixuebao.2021269

Li, K. W., Bian, H. Y., Liu, C. W., Zhang, D. F., and Yang, Y. N. (2015). Comparison of geothermal with solar and wind power generation systems. *Renew. Sustain. Energy Rev.*, *42*, 1464–1474. https://doi.org/10.1016/j.rser.2014.10.049

Li, Q. (2015). Hydrochemistry and evaluation of geothermal water in Yuncheng. *J. Water Resour. Architect. Eng. (in Chinese)*, *13*(5), 127–130,184. https://doi.org/10.3969/j.issn.1672-1144.2015.05.025

Li, Z., Feng, Z. Q., Hou, J. B., Guo, L. L., He, J. C., Wang, Q., Hao, S. Q., and Deng, Y. L. (2023). The law of geothermal resources in Shanxi Province and its geological background. *Geol. Explor. (in Chinese)*, *59*(2), 353–376. https://doi.org/10.12134/j.dzykt.2023.02.012

Li, Z. H., Liu, B. J., Yuan, H. K., Feng, S. Y., Chen, W., Li, W., and Kou, K. P. (2014). Fine crustal structure and tectonics of Linfen Basin—from the results of seismic reflection profile. *Chinese J. Geophys. (in Chinese)*, *57*(5), 1487–1497. https://doi.org/10.6038/cjg20140513

Liu, H. Y., Peng, C., Xue, L. F., Li, W. Q., Xu, C. H., and Jofrisse, C. S. (2022). Non-seismic geophysical analysis of potential geothermal resources in the Longgang Block, Northeast China. *Earth Planet. Phys.*, *6*(6), 576–591. https://doi.org/10.26464/epp2022046

Moeck, I. S. (2014). Catalog of geothermal play types based on geologic controls. *Renew. Sustain. Energy Rev.*, *37*, 867–882. https://doi.org/10.1016/j.rser.2014.05.032

Muñoz, G. (2014). Exploring for geothermal resources with electromagnetic methods. *Surv. Geophys.*, *35*(1), 101–122. https://doi.org/10.1007/s10712-013-9236-0

Neri, M., Ferrera, E., Giammanco, S., Currenti, G., Cirrincione, R., Patanè, G., and Zanon, V. (2016). Soil radon measurements as a potential tracer of tectonic and volcanic activity. *Sci. Rep.*, *6*, 24581. https://doi.org/10.1038/srep24581

Peng, R. H., Zhou, W. L., Hu, X. Y., Liao, W. Y., Wei, M. H., and Zhang, C. S. (2023). 3D inversion of multifrequency controlled-source electromagnetic data and its application to geothermal exploration in the Tianzhen region of the northern Datong Basin, China. *Geophysics*, *88*(6), E173–E187. https://doi.org/10.1190/geo2022-0659.1

Qi, Y., Luo, J. H., Wu, J. D., and Chen, F. K. (2016). Geochemical and Sr-Nd-Pb isotopic composition of the Canfang and Gufengshan granodiorite plutons in central-southern North China. *Acta Petrol. Sin. (in Chinese)*, *32*(7), 2015–2028.

Qiao, J. W., Peng, J. B., Deng, Y. H., Leng, Y. Q., and Meng, Z. J. (2018). Earth fissures in Qinglong Graben in Yuncheng Basin, China. *J. Earth Syst. Sci.*, *127*, 10. https://doi.org/10.1007/s12040-017-0912-1

Rao, S., Jiang, G. Z., Gao, Y. J., Hu, S. B., and Wang, J. Y. (2016). The thermal structure of the lithosphere and heat source mechanism of geothermal field in Weihe Basin. *Chinese J. Geophys. (in Chinese)*, *59*(6), 2176–2190. https://doi.org/10.6038/cjg20160622

Ren, Z. L., Liu, R. C., Ren, W. B., Qi, K., Yang, G. L., Cui, J. P., Yang, P., and Zhang, Y. Y. (2020). Distribution of geothermal field and its controlling factors in the Weihe basin. *Acta Geol. Sin. (in Chinese)*, *94*(7), 1938–1949. https://doi.org/10.19762/j.cnki.dizhixuebao.2020220

Rizzello, D., Armadillo, E., Pasqua, C., Pisani, P., Balsotti, R., Kebede, S., Mengiste, A., Kebede, Y., Hailegiorgis, G., and Mengesha, K. (2021). The geophysical recognition of a vapor-cored geothermal system in divergent plate tectonics: The Alalobeda (Alalobad) field, Ethiopia. *Tectonophysics*, *813*, 228933. https://doi.org/10.1016/j.tecto.2021.228933

Rizzello, D., Armadillo, E., Pasqua, C., Pisani, P., Principe, C., Lelli, M., Didas, M., Giordan, V., Mnjokava, T., Kabaka, K., Tumbu, L., and Marini, L. (2022). Assessment of the Kiejo-Mbaka geothermal field by three-dimensional geophysical modelling. *Geomech. Geophys. Geo.*, *8*(5), 143. https://doi.org/10.1007/s40948-022-00456-5

Seyis, C., İnan, S., and Streil, T. (2010). Ground and indoor radon measurements in a geothermal area. *Acta Geophys.*, *58*(5), 939–946. https://doi.org/10.2478/s11600-010-0012-y

Scott, M., and Mykle R. (2001). ZONGE data processing two-dimensional, smooth-Model CSAMT Inversion version 3.00. Zonge, Tuscon, AZ: Zonge Engineering and Research Organization, Inc.

Sun, J. L., Liu, K., He, Q. C., Yu, T. X., and Deng, Y. F. (2022). Thermal infrared remote sensing and soil gas radon for detecting blind geothermal area. *Geothermics*, *105*, 102534. https://doi.org/10.1016/j.geothermics.2022.102534

Sun, J. Y. (2016). The causes of gravity and magnetic anomaly in Yuncheng Basin and its adjacent area (pp. 1–63) [Master thesis] (in Chinese). Xi'an: Xi'an Shiyou University.

Susilawati, and Mustopa, E. J. (2019). 2D Interpretation of Controlled Source Audio Magnetotelluric (CSAMT) data integrated with borehole data in Kamojang geothermal field west Java, Indonesia. *J. Phys.: Conf. Ser.*, *1127*, 012021. https://doi.org/10.1088/1742-6596/1127/1/012021

Taylor, G., and Eggleton, R. A. (2001). *Regolith Geology and Geomorphology*. Chichester, UK: John Wiley and Sons.

Torres-Verdín, C., and Bostick, F. X. (1992). Principles of spatial surface electric field filtering in magnetotellurics: Electromagnetic array profiling (EMAP). *Geophysics*, *57*(4), 603–622. https://doi.org/10.1190/1.1443273

Ussher, G., Harvey, C., Johnstone, R., Anderson, E., and Zealand, N. (2000). Understanding the resistivities observed in geothermal systems. In *Proceedings World Geothermal Congress* (pp. 1915–1920). Kyushu-Tohoku, Japan.

Wang, G. L., Zhang, W., Liang, J. Y., Lin, W. J., Liu, Z. M., and Wang, W. L. (2017). Evaluation of geothermal resources potential in China. *Acta Geosci. Sin. (in Chinese)*, *38*(4), 449–459. https://doi.org/10.3975/cagsb.2017.04.02

Wang, G. L., and Lin, W. J. (2020). Main hydro-geothermal systems and their genetic models in China. *Acta Geol. Sin. (in Chinese)*, *94*(7), 1923–1937. https://doi.org/10.19762/j.cnki.dizhixuebao.2020224

Wang, H. Y., Wu, G. P., Chen, G. X., Chai, J. Z., Mao, J., and Wang, D. T. (2025). Microtremor survey-based investigation of deep geothermal- and water-controlling structures in the Salt Lake geothermal field, Yuncheng City, Shanxi Province, China. *Geophys. Geochem. Explor. (in Chinese)*, *49*(1), 32–40. https://doi.org/10.11720/wtyht.2025.1327

Wu, G. P., Chen, G. X., Chai, J. Z., Mao, J., Wang, H. Y., and Wang, D. T. (2025). Study on the spatial characteristics and controlling factors of subsurface temperature field in concealed Salt Lake geothermal reservoir, Yuncheng city, Shanxi Province, China. *Geothermics*, *131*, 103378. https://doi.org/10.1016/j.geothermics.2025.103378

Xie, C. L., Chen, C., Liu, C. G., Wan, W. T., Ye, S, Ye, G. F., Jin, J. N., and Yun, W. (2024). Insights from underground laboratory observations: attenuation-induced suppression of electromagnetic noise. *Eur. Phys. J. Plus*, *139*(3), 218. https://doi.org/10.1140/epjp/s13360-024-05033-1

Xing, Z. Y., Zhao, B., Tu, M. Y., and Xiong, J. S. (2005). The formation of the Fenwei rift valley. *Earth Sci. Front. (in Chinese)*, *12*(2), 247–262. https://doi.org/10.3321/j.issn:1005-2321.2005.02.027

Xu, H. R., Luo, Y. H., Yang, Y. J., Shen, W. S., Yin, X. F., Chen, G. X., Yang, X. Z., and Sun, S. D. (2020). Three-dimensional crustal structures of the Shanxi rift constructed by Rayleigh wave dispersion curves and ellipticity: Implication for sedimentation, intraplate volcanism, and seismicity. *J. Geophys. Res.: Solid Earth*, *125*(11), e2020JB020146. https://doi.org/10.1029/2020JB020146

Xu, X. W., and Ma, X. Y. (1992). Geodynamics of the Shanxi rift system, China. *Tectonophysics*, *208*(1-3), 325–340. https://doi.org/10.1016/0040-1951(92)90353-8

Xu, X. W., Ma, X. Y., and Deng, Q. D. (1993). Neotectonic activity along the Shanxi rift system, China. *Tectonophysics*, *219*(4), 305–325. https://doi.org/10.1016/0040-1951(93)90180-R

Yang, Y., Xiong, B., Peng, S. X., Chen, H. B., Zhang, T. Y., and Liu, L. (2023). Geothermal exploration using numerical simulation and a comprehensive electromagnetic method. *Petrol. Sci. Technol.*, *41*(3), 361–385. https://doi.org/10.1080/10916466.2022.2060256

Yin, Y. T., Jin, S., Wei, W. B., Ye, G. F., Jing, J., Zhang, L. T., Dong, H., Xie, C. L., and Liang, H. D. (2017). Lithospheric rheological heterogeneity across an intraplate rift basin (Linfen Basin, North China) constrained from magnetotelluric data: Implications for seismicity and rift evolution. *Tectonophysics*, *717*, 1–15. https://doi.org/10.1016/j.tecto.2017.07.014

Zarrouk, S. J., and McLean, K. (2019). *Geothermal Well Test Analysis: Fundamentals, Applications and Advanced Techniques*. Hoboken: Academic Press.

Zhang, Y. Q., Liao, C. Z., Shi, W., Zhang, T., and Guo, F. G. (2007). Jurassic deformation in and around the Ordos Basin, North China. *Earth Sci. Front.*, *14*(2), 182–196. https://doi.org/10.1016/S1872-5791(07)60016-5

Zhang, Y. Q, Xiao, Y., Yang, H. J., Wang, S. B., Wang, L. W., Qi, Z. X., Han J. B., Hao Q. C., Hu W. X., and Wang, J. (2024). Hydrogeochemical and isotopic insights into the genesis and mixing behaviors of geothermal water in a faults-controlled geothermal field on Tibetan Plateau. *J. Clean. Prod.*, *442*, 140980. https://doi.org/10.1016/j.jclepro.2024.140980

Zhao, B. (2013). Volcano- magma-mineralization processing and metallogenic prediction of Dazhongtiao area (pp. 1–20) (in Chinese). Xi'an: Chang'an University.

Zhao, G. C., Sun, M., Wilde, S. A., and Li, S. Z. (2005). Late Archean to Paleoproterozoic evolution of the North China Craton: key issues revisited. *Precambrian Res.*, *136*(2), 177–202. https://doi.org/10.1016/j.precamres.2004.10.002

Zhou, W. L., Hu, X. Y., Yan, S. L., Guo, H. D., Chen, W., Liu, S. J., and Miao, C. Y. (2020). Genetic analysis of geothermal resources and geothermal geological characteristics in Datong Basin, Northern China. *Energies*, *13*(7), 1792. https://doi.org/10.3390/en13071792

Zhou, W. L. (2021). Electrical structure of geothermal area in northeast of Datong Basin [Ph. D. thesis] (in Chinese). Wuhan: China University of Geosciences. https://doi.org/10.27492/d.cnki.gzdzu.2021.000010

Zhou, W. L., Hu, X. Y., Guo, H. D., Liu, S., Liu, S. J., and Yang, B. (2022). Three-dimensional magnetotelluric inversion reveals the typical geothermal structure of Yanggao geothermal field in Datong Basin, northern China. *Geothermics*, *105*, 102505. https://doi.org/10.1016/j.geothermics.2022.102505

Zhu, J. L., Hu, K. Y., Lu, X. L., Huang, X. X., Liu, K. T., and Wu, X. J. (2015). A review of geothermal energy resources, development, and applications in China: Current status and prospects. *Energy*, *93*, 466–483. https://doi.org/10.1016/j.energy.2015.08.098